

An Observation of the Intermediate Polar XY Arietis with Chandra

A. Salinas^{1,2,3} & E. M. Schlegel²

ABSTRACT

Chandra serendipitously observed the eclipsing ($80^\circ < i < 84^\circ$) intermediate polar, XY Arietis (=H0253+193), in two separate but continuous observations five weeks apart. XY Ari was in a quiescent state during both observations. We pursue the study of phase-resolved spectra for this system focusing on the Fe K lines. From the combined and separate data sets, we readily detect emission lines of iron near 6.4, 6.7, and 6.9 keV at better than 99% significance in contrast to previous results. We confirm the orbit-phased sinusoidal absorption column behavior first observed with Ginga as well as a sinusoid-like behavior as a function of spin phase. The presence of the 6.4, 6.7, and 6.9 keV lines requires different ionization states with $\xi < 2$ (6.4 keV) and $\xi \sim 3.5$ –4 (6.7 and 6.9 keV) that must vary with phase. We also detect emission lines at 3.25, 4.8, and 5.4 keV that are not instrumental in origin. The 4.8 keV line may be identified as Ca XIX (4.832 keV) and the 3.25 keV line may be Ar I K, but the 5.4 keV line has no obvious identification.

Subject headings: (stars:) cataclysmic variables; Xrays: binaries; stars: individual (XY Ari)

1. Introduction

XY Ari belongs to the class of binary stars known as cataclysmic variables (CV's) which are characterized by mass transfer between a red dwarf and a white dwarf (Warner 1995). The infalling mass may create an accretion disk surrounding the white dwarf depending on the strength of the magnetic field of the primary star. CV's in which the primary has little to no magnetic field have large accretion disks; systems for which the white dwarf has a large magnetic field (polars or AM Her stars)

do not have an accretion disk and matter accretes onto one pole of the primary. XY Ari is a member of the intermediate polar subclass (=IP or DQ Her stars; Patterson 1994). These stars may have both a magnetic field and an accretion disk, but debate exists on the degree of disk versus diskless accretion (e.g., Norton et al. 1997). In either scenario, the mass transfer material accretes onto the magnetic poles of the white dwarf; the differences in the scenarios lie in the type of the accretion, whether arc-like (disk-fed) or funnel-like (stream-fed) and the consequently different observational signatures expected from the two methods (e.g., Norton, Beardmore, & Taylor 1996 for power spectra).

XY Ari is the only fully eclipsing interme-

¹University of Texas, Austin, TX

²Harvard-Smithsonian Center for Astrophysics, Cambridge, MA

³NSF REU student

diate polar known¹; as luck would have it, the CV is hidden behind a molecular cloud, Lynds 1457, and is virtually invisible in the optical (visual extinction of $A_v = 11.5 \pm 0.3$; Littlefair, Dhillon, & Marsh 2001). Kamata, Tawara, & Koyama (1991) determined XY Ari’s X-ray spin period, ω , = 206.298 \pm 0.001 s, and its orbital period Ω , to be 21,829 \pm 3 s (\approx 6.02 h), thereby firmly establishing its classification as an IP. Hellier (1997) observed XY Ari during its only known outburst and placed a limit on the accretion region of <0.002 of the white dwarf’s surface area, as well as constraining the inclination of the system to be $80^\circ < i < 84^\circ$.

The continuum emission of these systems provides the overall properties (e.g., inclination, eclipse width, column absorption, etc.), while the line emission has the potential to provide specific details (e.g., temperatures, electron densities, emitting region visibility). Of particular interest are the emission lines of iron in the 6-7 keV band. Previous studies of the lines studied their behavior over the entire observation at CCD resolution (Ezuka & Ishida 1999, Hellier, Mukai, & Osborne 1998) or at grating resolution (e.g., Mukai et al. 2003). Previous time-resolved studies of the X-ray emission focused solely on the continuum (eg., Kamata & Koyama 1993; Norton & Watson 1989). In our study of XY Ari using archival Chandra data, we focus on the time-resolved behavior of the iron lines in the 6.4-6.9 keV region.

2. Observation

Chandra observed XY Ari on 2000 July 9-10 for approximately 56 ksec and then again on 2000 August 17 for approximately 44 ksec (obs id: 943, target name: MBM12). Chan-

dra observations of length less than ~ 150 ksec are usually scheduled in one continuous pass at the object; the July 2000 observation was interrupted by high solar radiation and the remaining time was re-scheduled for mid-August. A few ksec were trimmed off the end of the first observation by the automated data processing because of violations of background count rates. The data were completely re-processed during an overall CXC re-processing effort in 2001-2002 that improved various calibration-related issues. We obtained the re-processed data from the archive.

Both observations placed XY Ari on the Advanced CCD Imaging Spectrometer (ACIS)-S3 chip; the aim point on the S3 chip serendipitously placed XY Ari ~ 5.6 arcmin off-axis. The off-axis position mitigates the effects of event pile-up not only from the reduced effective area ($\sim 86\%$, CXC Proposers’ Observatory Guide 2002) but also from the broader point spread function (=PSF; ~ 2 times larger than on-axis as defined by the 90% encircled energy behavior). To verify that the source was free of pile-up, we generated a radial profile of the source for the entire ~ 100 ks and compared it to the theoretical PSF. For the profiles, we centered a series of 30 annuli 0.49 arcseconds apart on the source and sampled the background with an annulus of inner radius 16 arcseconds and outer radius of 30 arcseconds. We used the CIAO (Chandra Imaging and Analysis of Observations v2.2.1)² tools to extract the counts in each annulus to construct the profile. For the theoretical PSF, we used the `mkPSF` tool in CIAO and then normalized the result by the total number of counts in the source region. Both the theoretical and observed profiles agreed to within 0.4%. Agreement between the profiles, particularly in and near the center, indicates little or no pileup exists in the source.

¹Although Singh & Rana (2003, A&A, 410, 231) argue that the eclipsing CV V1432 Aql is an IP; if confirmed, our use of “only” would be no longer correct.

²<http://asc.harvard.edu/ciao/>

The observations of XY Ari, although separated in time, occurred within a few weeks of each other. As a result, the time-dependent gain changes described in Vikhlinin et al. (2003)³ do not alter the energy scales assigned to the two observations as the differences in the gains between the two observations were insignificant.

Shown in Figure 1 are light curves for both observations using bins of width 90 s in the energy range of 0.3-10 keV. We removed 1.2 ksec of time from the first observation in which the background significantly increased, most likely caused by an increase in the charged particle background induced by a solar flare. The times were corrected to the solar barycenter using the CIAO code `axbary` with the DE405 solar system ephemeris (consistent with the ICRS reference system). We then determined the source count rates for both observations by centering a circle of radius of 0.14 arcminutes at the source position. Background counts were accumulated from an annulus surrounding the source using an inner radius of 0.27 arcminutes and an outer radius of 0.54 arcminutes. The source had a count rate of 0.346 counts s⁻¹ (flare-subtracted data) with a background rate of 0.0093 counts s⁻¹ during the first observation and source and background rates of 0.302 counts s⁻¹ and 0.0096 counts s⁻¹, respectively, during the second observation.

2.1. Orbit Period

Two full orbital cycles of XY Ari are covered by the two observations. We folded the light curve on the orbital period using the ephemeris of Allan, Hellier, & Ramseyer (1996). Within the errors, the predicted values match the observed eclipse times. We do not show the orbital light curve because

³The web address for this reference is <http://www.harvard.edu/~alexey/acis/tgain/>.

most of the features may be inferred from Figure 1. Table 1 lists the mid-eclipse times determined from the half-point at 50% of the eclipse depth. We also examined the hardness ratios phased at the orbital period; we do not present the ratios here since they are constant within the errors over the orbital period.

2.2. Spin Period

Hellier (1997) used an ephemeris that started at TDB 245 0277.40382 and adopted the Kamata et al. spin period. We adopted the same ephemeris and folded the data on that ephemeris as shown in Figure 2. A hardness ratio, defined as $HR = 4-8 \text{ keV} / 1-4 \text{ keV}$ was generated for each observation and is displayed in the lower portion of Figure 2. A representative error bar is also included. The two observations are similar, but the width of the pulse peak is significantly broader in the second observation (0.15 vs. 0.20).

Previous observations of XY Ari by Hellier (1997) studied the spin pulse profile, and the spin pulse profiles in this observation resemble those results. The absolute spin pulses in the Chandra observation are offset from earlier lightcurves by ≈ 0.32 phase shift in the first observation, and by ≈ 0.30 phase shift in the second observation. These offsets most likely originate with an error in the extrapolated ephemeris⁴. The profiles are essentially unchanged in shape which, for our purposes, is more important. We attempted to improve the ephemeris, but could not be certain of the cycle count.

2.3. Spin-Orbit behavior

Shown in Figure 3 are light curves, filtered into 3 orbit-phased bins, folded on the spin period, and separated into 2 energy bands (0.5-4.0 and 4.0-8.0 keV). Phases immediately at

⁴See Hellier (1997) for more discussion on the error in the ephemeris.

or adjacent to the eclipse were not included. We note the peak near spin phase 0.4 that is visible in the soft band, but not the hard band. The hard band light curves are essentially consistent with constant emission at all spin and orbit phases.

The count rate in the soft band (0.5-4.0 keV) during orbital phases 0.05-0.35 lies ~ 10 -15% above the count rates in the other bins. The corresponding hard band does not show such an increase. Otherwise, within the errors the bins behave nearly identically as a function of energy.

3. Data Analysis

3.1. General Spectral Fitting

This section provides overall details on the spectral fitting. Before commencing any spectral fits, we corrected the data for the low-energy contamination buildup (Plucinsky et al. 2003) and constructed a response matrix appropriate for the specific detector and the off-axis position of XY Ari. Spectra were extracted using the same apertures as defined for the light curves (§ 2). All spectra were fit with Sherpa v2.2.1 (Freeman, Doe, & Siemiginowska 2001) and Xspec v11.2 (Arnaud 1996) using χ^2 data variance. In each case, the continuum model was fit first with the expected regions of line emission masked. The line masks were then removed and fits to the line regions were carried out.

Previous fits to X-ray spectra of XY Ari used absorbed thermal bremsstrahlung models with $kT=16$, 17, and 30 keV (ASCA, Ginga, and RXTE observations respectively, Hellier 1997; Ezuka & Ishida 1999). Fits to the continuum of the ACIS data using a thermal bremsstrahlung model, a power law model, and a blackbody model all produced χ^2 values of ~ 1.1 . As our primary goal is the study of line variations, we require a good but simple fit to the continuum to de-

fine the lines. We adopted an absorbed thermal bremsstrahlung model not only to provide that simple fit but also for comparison with previous results.

The Chandra data do not constrain the bremsstrahlung temperature because of the relatively high values for the temperature typical of IPs and because of the declining effective area of the Chandra mirrors above ~ 5 keV. We adopted a temperature of 30 keV as determined from RXTE data because it has a broader bandpass than other satellites such as Ginga or EXOSAT that have observed XY Ari.

There are two different approaches for fitting lines, each with its own merits: (i) place gaussians at the positions of known lines and integrate the flux falling under the line; (ii) fit gaussians to detected lines. The first approach has the advantage of extracting the most information with the least degree-of-freedom cost since the line center is fixed. This approach has the drawback that the placed lines may not be statistically independent. The second approach is robust, but risks missing weak lines that fall below a predetermined significance threshold because of the extra degree-of-freedom cost.

We adopted the second approach because of the inherent resolution of the ACIS detector. We added as many gaussian lines as permitted by the statistical improvement of the fit and the statistical independence of the added line. Based upon X-ray observations using the Chandra High Energy Grating which shows narrow emission lines, the lines are expected to be unresolved in the ACIS data (Hellier & Mukai 2004; Mukai et al. 2003). Therefore, each added gaussian had its line width fixed at zero to mimic an unresolved line.

We calculated upper limits to any absent lines by adding a zero-width gaussian at the line's position, then raising the gaussian nor-

malization until $\Delta\chi^2$ changed by the required amount. In general, we quote 95% upper limits, hence the required change was 4.0 for 1 parameter of interest (the line strength); for comparison with values in the literature, we also use 1σ errors and explicitly state when we do so.

The original Chandra data were obtained in two separate observations. To reach the most sensitive detections for any line, we combined the observations to maximize the signal-to-noise which will henceforth be referred to as the 'combined data'. We subsequently fit each observation separately to detect any line strength variations over the five-week separation between the observations. We also broke each observation into phase bins as detailed below.

3.2. Overall Spectral Features

From the combined data, we extracted the source and background spectra in the same manner as described above for the light curves. This extraction was possible because XY Ari was in the same location on the CCD to within a few pixels. The total source spectrum was binned to 25 counts per channel and is shown in Figure 4. Lines near 6.4, \sim 6.7, and 6.9 keV are visible; in addition, a weak line at \sim 8.2 keV is also marginally detected. We henceforth use these designations to label the lines. We identify the strong lines as Fe I $K\alpha$ at 6.39 keV, the Fe XXV triplet complex in the 6.64-6.70 keV band, and Fe XXVI $Ly\alpha$ 6.96 keV.

We then analyzed each data set separately. For the separate observations, we binned the spectra to 15 counts per channel. We do not show the spectra because they are visually similar to Figure 4. Both observations separately show emission lines at 6.4, 6.7, and 6.9 keV with significance $>99\%$. The absorption was also significantly higher during the second observation. The results from the fits

to the combined and separate data sets are in Table 2.

3.3. Phase-Resolved Fits and Results

The count rate from XY Ari is sufficiently high to allow a study of the time-resolved line emission, both at orbital and spin phases, but sufficiently low to force considerations of the signal-to-noise per phase bin.

Intermediate polars are generally not studied at orbital phases because of the inherent blending of spin-dependent features. In Kamata & Koyama (1993), the authors published a plot of the orbital-dependent behavior of the absorption column, reporting a sinusoidal-like behavior. Figure 6 shows the orbit-phased behavior of the absorption column using 5 orbital phase bins for each observation. We confirm the variable behavior with orbital phase.

For the spin-phased spectroscopy, we settled on two approaches. First, based upon Figure 3, spin phases \sim 0.3-0.6 contain a peak visible at all orbital phases. We divided the data into 3 bins phased on the spin period to study any orbital-dependent differences directly. Table 3 lists the results for the 3-bin fits. Second, we divided the data into 5 bins again phased on the spin period to push the phase resolution as much as possible; table 4 lists the results for the 5-bin fits. Examples of two spectra from the 5-bin fits are shown in Figure 5 and illustrate significant variations in line strengths.

Figure 7 shows the changes in the absorption column throughout each observation and using the results from the 5-bin set of data phased at the spin period. The absorption is lowest at the spin phases that correspond to low hardness ratios, and highest when there is a peak in the hardness ratio. This behavior matches the model of additional matter along the line of sight at specific spin phases, simi-

lar to a recent analysis of X-ray spectra of the IP PQ Gem James et al. (2002); the added matter most likely originates from the accretion stream or arc. Alternatively, a second, soft emission component could become visible during those phases and leading to a smaller fitted value for the column density. The spectral fit does not require an additional emission component, however.

The 6.4 keV line differs between the two observations and appears to vary within an observation (Figure 8). A survival statistics analysis confirms our impressions (Lavalley, Isobe, & Feigelson 1992). For the 6.4 keV line, the probability is low (~ 0.03) that the equivalent widths from the two observations arise from the same parent population. The probability estimate is robust in that three different survival tests (generalized Wilcoxon, Kaplan-Meier estimator, log rank test) each yield similar probabilities (0.025, 0.033, 0.049, respectively). The 3- and 5-bin mean Kaplan-Meier estimates yield approximately a factor of 2 difference between the observations over the 5-week gap for the 6.4 keV lines. The 5-bin mean values are 141 ± 25 eV and 72 ± 4 eV for the first and second observations, respectively. This represents a real detection of differing line strengths in the 6.4 keV line.

Weak evidence exists for line variations in the 6.7 keV region (Figure 8). The Kaplan-Meier estimates state that the mean values are essentially identical at 148 ± 31 and 131 ± 15 eV for the first and second observations, respectively; the 3-bin Kaplan-Meier values are identical. However, a fit of a constant or a linear decline shows that a decline provides a marginally better fit with $\Delta\chi^2$ decreasing by 2.7 which is significant at 90% for the extra degree-of-freedom.

For the 6.96 keV line, the line fluxes are constant with phase within the errors; the Kaplan-Meier estimates of the means differ but are just short of overlapping at 120 ± 15

and 86 ± 17 eV. The probability that the two samples were drawn from the same population is ~ 10 -12%. Higher signal-to-noise spectra will be needed to verify or refute any possible line variability.

3.4. Unexpected Emission Lines

We also detected three emission lines in the first observation, each at relatively large significance, that appear in the ~ 3 -6 keV band and are not normally observed in astrophysical sources (Table 5). The first line appears in the 0.2-0.4 phase bin at 3.25 keV with $\sim 94\%$ significance, the second at 4.81 keV in the phase 0.8-1.0 bin with $>99\%$ significance (visible in Figure 5), and the third lies at 5.39 keV in the 0.0-0.2 phase bin with a significance of $\sim 97\%$. We expended considerable effort to understand their nature, as yet without success.

The Chandra calibration team has shown no line in the background at any of the three detected line energies. The XY Ari background data do not show emission at these energies. We applied current gain maps to the files during their initial re-processing, so the lines are not artifacts of the processing or the use of old gain values. During the orbit phases where the lines are seen, we filtered the data on energy, isolating each line. Images of the results show each line centered on the position of XY Ari, which is counter to the expectation that the lines arise from the background.

If we ignore the 0.5 keV difference in line energy for the moment, the 5.39 keV line could result from contamination from on-board calibration sources, in which X-rays hitting the calibration devices proceed to the detector and contaminate the data. The Mn K α calibration source emits at 5.9 keV; the line is easily visible in event histogram data (an instrument mode used for ACIS calibration), but these data are collected *only* when ACIS is *not* in the focal plane (Chandra Cal-

ibration team 2002). The cal source might explain the line if the line were present at all phases; the line, however, is *not* so cooperative. The line is essentially visible in a single phase bin.

Another possibility exists: the lines are red- or blue-shifted from their rest energies. Without a firm identification for each line, we can not calculate velocities. If we assume the lines are red-shifted Fe K emission, the velocities involved are very large. Adopting a rest energy of 6.40 keV, we obtain velocities in the range of 0.2c-0.5c for the three lines, values well beyond the capabilities of the potential well of a white dwarf.

Finally, charged particle events create emission lines in the background spectrum from X-ray fluorescence of materials in the detector. If we take the fitted line centers as fluorescing lines, then the 3.25 keV line might be attributed to Ar K α (3.20 keV) and the 5.39 keV line to Cr Ka (5.41 keV). The error on the line center of the 3.25 keV line is sufficiently large that it encompasses several ionization states of Ar.

The 4.81 keV line does not match any K line, as is expected for X-ray fluorescence; possible matches regardless of mechanism are ^{53}I L γ (4.80 keV), ^{56}Ba L β (4.83 keV), but both lines are very weak (Kortright & Thompson 2001); the identification is not plausible given the low abundance of these elements. A more plausible identification for the 4.81 keV line is Ca XIX with rest energy 4.823 keV. The error on the line center of the 4.81 keV line easily encompasses this rest energy and the abundance of Ca is sufficiently high that the identification appears robust. This is apparently the first detection of Ca XIX in any CV.

The 3.2 keV line, associated with Ar K α above, also has observational support: the *ASCA* spectrum of the intermediate polar EX Hya shows emission from Ar XVII K α and XVIII K α lines at 3.125 and 3.319 keV,

respectively (Fujimoto & Ishida 1997). The equivalent widths were measured as ~ 20 eV each, broadly consistent with unresolved emission in the ACIS spectrum if we assume the two systems have similar radiation environments.

4. Discussion

XY Ari was in quiescence during the Chandra observation. The Einstein, Ginga, and quiescent RXTE luminosities L_X were ~ 1.7 , ~ 3.5 , and ~ 2.6 , respectively, in units of 10^{32} erg s $^{-1}$ in the 2-10 keV band (Patterson & Halpern 1990; Kamata & Koyama 1993; Hellier, Mukai, & Beardmore 1997). These luminosities have been corrected for distance, from the originally published values based on a distance of ~ 65 pc (Patterson & Halpern 1990) to the more recent estimate of 270 ± 100 pc (Littlefair, Dhillon, & Marsh 2001). The mean Chandra luminosity is $3.1 \pm 0.1 \times 10^{32}$ erg s $^{-1}$.

We fit three different spectral data sets for XY Ari: the combined data, the summed spectra for each observation separately, and the phase-resolved spectra for each observation. We discuss each in turn.

The lines detected in the combined data are at first glance similar to the previous spectral studies using *ASCA* (Hellier, Mukai, & Osborne 1998; Ezuka & Ishida 1999). However, the Hellier et al. study confidently detected only the 6.7 keV line; the 6.4 and 6.9 keV lines in their table are really upper limits. Similarly for Ezuka & Ishida: they list three lines in their table, but they detect the 6.4 keV line with 90% confidence and report upper limits for the 6.7 and 7.0 keV lines. In contrast, we detect three lines at $>99\%$ confidence in the combined data and in each observation separately (Table 2). The differences in the detections among the various studies may be attributed to variations in the signal-to-noise

of the corresponding spectra, but may also indicate variability in line fluxes as a function of time. If the lines vary, then significant clues to the detailed accretion physics await detection of the variations as a function of spin phase.

The presence of the 6.4, 6.7, and 6.9 keV lines provides constraints on the ionization parameter $\xi = L_X / R^2 n$, where R is the size of the emitting region and n is the number density. The 6.4 keV fluorescent line appears if $\xi < 2$ (Kallman & McCray 1982) and requires an ionization stage of XVI or smaller. The 6.7 and 6.9 keV lines, however, arise from Fe XXV and XXVI, respectively, and require a higher ionization state. For the few phases where the lines are equally detected, (e.g., observation 1, phases ~ 0.3 and ~ 0.7), the 6.7/6.9 line strength ratio of ~ 1 (range: 0.6 to 1.3) implies $\xi \sim 3.5$ –4. The upper limits on these lines, particularly for observation 2, phase ~ 0.1 , require considerable variation in the ionization state with spin phase.

Following Bautista & Titarchuk (1999), for temperatures below ~ 12 keV, there is essentially zero emission from Fe XXVI Ly α . The upper limits on the line emission, particularly the more restrictive limits of observation 2, require either a multi-temperature plasma or significant blockage of the line emission; the latter inference requires a contrived geometry to remove line emission without also removing continuum emission. Multi-temperature plasmas in the accretion columns of IPs emerged from applications of the models of Aizu (1973); early spectral fits required only a single temperature. Multi-temperature plasmas were first demonstrated from spectral fits by Ishida, Mukai, & Osborne (1994) using *ASCA* data. The conclusion presented here is therefore not new, but it confirms the physics using phase-resolved spectroscopy of emission lines. The emission from the lines should be nearly co-located, in contrast to an alternative explanation of the Ishida, Mukai, & Osborne

(1994) results, namely that the line source regions were widely distributed.

The strength of the 6.4 keV line is proportional to the column density of material (Kallman 1995): $E_{\text{FWHM}} \sim 2.3 N_{24}$ keV, where N_{24} is the column density in units of 10^{24} cm^{-2} . The measured mean values imply a factor of ~ 2 change in the column density. The line strength is also related to the inclination because of the increasing path length through the disk for higher-inclination systems (van Teeseling, Kaastra, & Heise 1996). From figure 4 of the van Teeseling et al. paper and for a specified inclination, a change in the 6.4 keV equivalent width requires either a change in the bremsstrahlung temperature or other processes, such as optical depth effects or temperature inversions.

That the 6.4 keV fluorescence line is only detected at specific spin phases will presumably tell us more about asymmetries in the cold iron gas surrounding the accretion region. Variations in ionization state likely arise from aspect variations of the accretion region, non-uniform filling factors of the absorbing gas, or optical depth effects. We know line emission occurs preferentially in directions low optical depth; variations in optical depth could easily affect the inferred phase-dependent effects reported here. High wavelength- and time-resolution observations will be necessary to sort out optical depth effects.

We conclude with several speculative comments.

The apparently transient behavior of the 4.8 keV line may be described as flare-like. Ca XIX is detected in solar flares (e.g., Fludra & Schmelz 1999); this line may represent the first such detection in CV.

The second observation showed marginal evidence for the presence of a line at ~ 6.25 keV. If the ‘line’ is actually a Compton shoulder on the Fe K α line arising from single-

scattered photons, then measurements of the column density of the scattering medium and its metal abundance may be possible (van Teeseling, Kaastra, & Heise 1996; Watanabe, S. et al. 2003).

The spectral fit of the first observation is improved by a line at ~ 7.1 keV, perhaps the Fe I $K\beta$ line; the $\beta : \alpha$ branching ratio is 17:150 (Bambynek et al. 1972). Similarly, the second observation detects a line at ~ 8.2 keV, possibly the $Ly\beta$ line of Fe XXVI. The decreasing effective area of the Chandra mirrors prevent robust detection of the continuum and any possible line(s) above ~ 7 keV, but provide two goals for spectroscopy of IPs using future X-ray observatories since both lines serve as temperature indicators.

We thank the referee for comments that materially improved the presentation. AS thanks everyone connected with the REU program for support. We thank Eli Beckerman for helping with aspects of the software. The research of EMS was supported by contract NAS8-39073 to the Smithsonian Astrophysical Observatory.

REFERENCES

- Aizu, K. 1973, *Prog Theor Phys*, 49, 1184
- Allan, A., Hellier, C., & Ramseyer, T. F. 1996, *MNRAS*, 282, 699
- Arnaud, K. 1996 in *ASP Conf Ser 101, Astronomical Data Software & Systems V*, ed. G. H. Jacoby & J. Barnes (San Francisco: ASP), 17
- Bambynek, W. et al. 1972, *RevModPhys*, 44, 716
- Bautista, M. A. & Titarchuk, L. 1999, *ApJ*, 511, 105
- Biller, B., Plucinsky, P., & Edgar, R. 2002, Chandra Calibration team, (<http://asc.harvard.edu/calLinksAcisacis>)
- Chandra Observatory Center Proposers' Observatory Guide, 2002, (Cambridge, MA: Smithsonian Astrophysical Observatory)
- Ezuka, H. & Ishida, M. 1999, *ApJS*, 120, 277
- Fludra, A. & Schmelz, J. T. 1999, *A&A*, 348, 246
- Freeman, P., Doe, S., & Siemiginowska, A. 2001, *SPIE*, 4477, 76
- Fujimoto, R. & Ishida, M. 1997, *ApJ*, 474, 774
- Hellier, C., Mukai, K., & Beardmore, A. P. 1997, *MNRAS*, 292, 397
- Hellier, C. 1997, *MNRAS*, 291, 71
- Hellier, C., Mukai, K., & Osborne, J. P. 1998, *MNRAS*, 297, 526
- Hellier, C. & Mukai, K. 2004, *MNRAS*, in press (astro-ph/0405254)
- Ishida, M., Mukai, K., & Osborne, J. P. 1994, *PASJ*, 46, L81
- James, C. H., Ramsay, G.; Cropper M.; Branduardi-Raymont, G. 2002, *MNRAS*, 336, 550
- Kallman, T. R. 1995, *ApJ*, 455, 603
- Kallman, T. R. et al. 1993, *ApJ*, 411, 869
- Kallman, T. R. & McCray, R. 1982, *ApJS*, 50, 263
- Kamata, Y. & Koyama, K. 1993, *ApJ*, 405, 307
- Kamata, Y., Tawara, Y., & Koyama, K. 1991, *ApJ*, 379, L65
- Kortright, J. B. & Thompson, A. C. 2001, in *X-ray Data Booklet* (Berkeley: Lawrence Berkeley National Laboratory)

Lavalley, M., Isobe, T., & Feigelson, E. 1992, Astronomical Data Analysis Software and Systems I, ASP Conference Series, Vol. 25, eds. D. M. Worrall, C. Biemesderfer, & J. Barnes, eds., 245

Littlefair, S. P., Dhillon, V. S., & Marsh, T. R. 2001, MNRAS, 327, 669

Mukai, K., Kinkhabwala, A., Peterson, J. R., Kahn, S. M., & Paerels, F. 2003, ApJ, 586, L77

Norton, A. J., Hellier, C., Beardmore, A. P., Wheatley, P. J., Osborne, J. P., & Taylor, P. 1997, MNRAS, 289, 362

Norton, A. J., Beardmore, A. P., & Taylor, P. 1996, MNRAS, 280, 937

Norton, A. J. & Watson, M. G. 1989, MNRAS, 237, 853

Patterson, J. 1994, PASP, 106, 209

Patterson, J. & Halpern, J. P. 1990, ApJ, 361, 173

Plucinsky, P. P. et al. 2003, Proc. SPIE, 4851, 89

van Teeseling, A., Kaastra, J. S., & Heise, J. 1996, A&A, 312, 186

Vikhlinin, A., Schulz, N., Tibbetts, K., & Edgar, R. 2003, Chandra calibration memo

Warner, B. 1995, Cataclysmic Variables (Cambridge: Cambridge Univ. Pr)

Watanabe, S. et al. 2003, ApJ, 597, L37

Table 1: Eclipse Times for XY Ari

Cycle	Relative Time (days)	BJD
0.0	0.0	2451735.108505
1.0	0.253472	2451735.361977
151.0	38.157035	2451773.26554
152.0	38.409875	2451773.51838

Fig. 1.— Lightcurves for the (top) first and (bottom) second observations of XY Ari with Chandra in the 0.3-10 keV band. Each bin is 90s in size. The first observation included a 1.2 ksec time span that was contaminated by a background-induced flare near 7959e7 that was excised from the data. The other four, broader drops in count rate are the XY Ari eclipses. Time is given in Chandra time, which is seconds from MJD=50814.

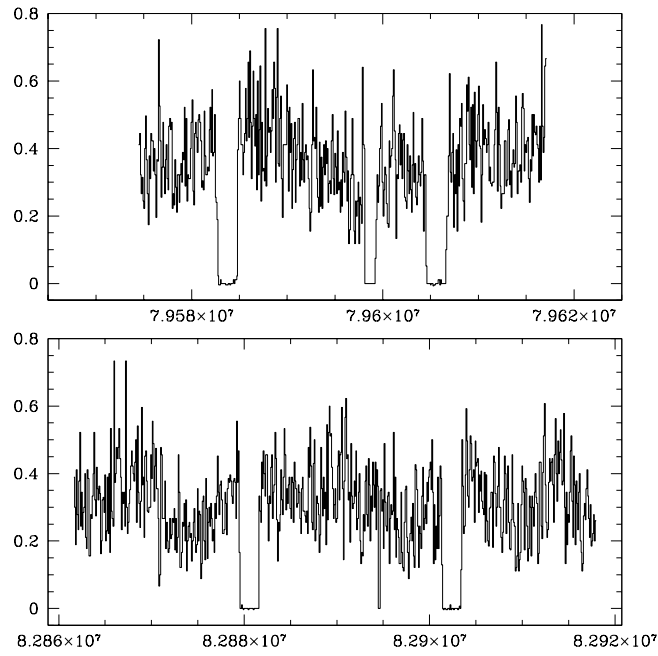


Fig. 2.— Spin period-folded lightcurves folded on the 206.298s spin period for both observations. Also shown are the 4-8 keV/1-4 keV hardness ratios. The data have been repeated twice for clarity.

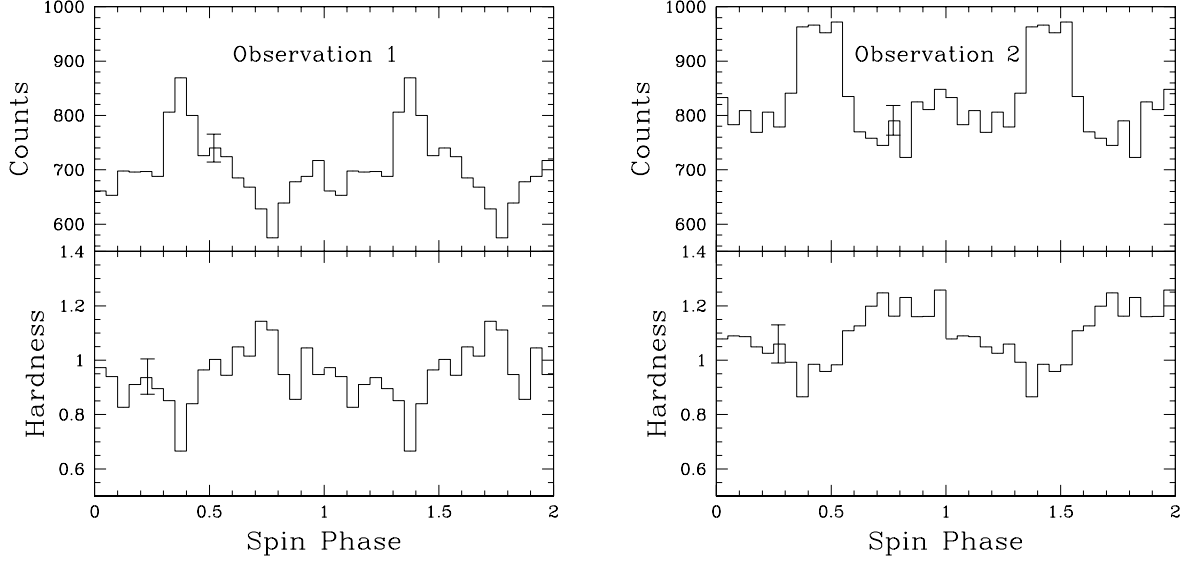


Fig. 3.— Orbit-phase data filtered into 3 phase bins for which each bin is folded on the spin period. Both the soft (0.5-4 keV) and hard (4-8 keV) bands are shown. The data are repeated twice for clarity.

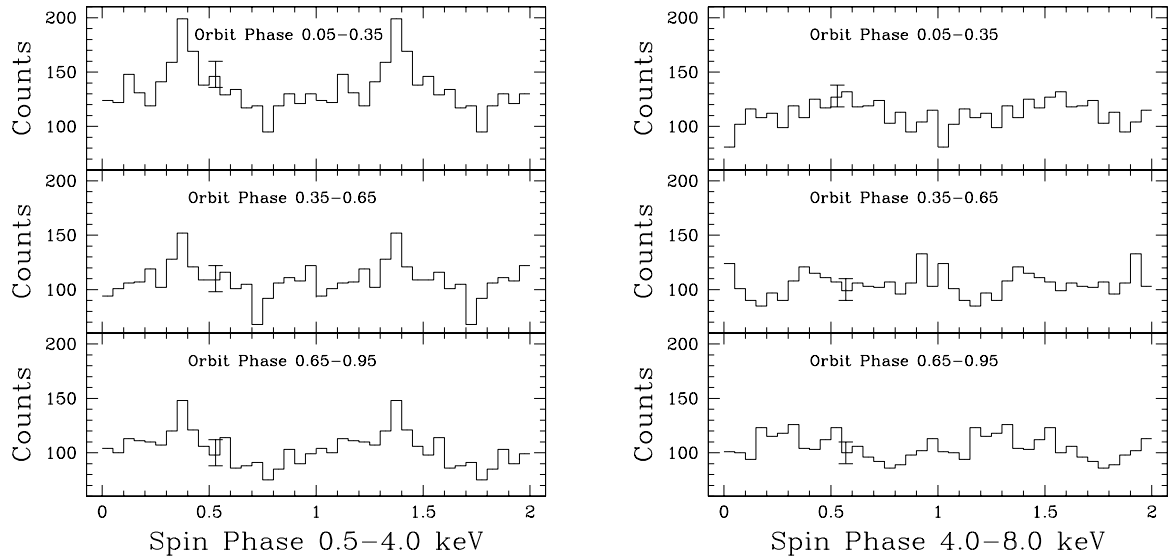


Fig. 4.— The fit to the combined data set. The emission lines have deliberately not been included in the fit so the emission region is more readily apparent. The region from 5.2 to 7.2 keV, including the fit, is shown expanded in the inset.

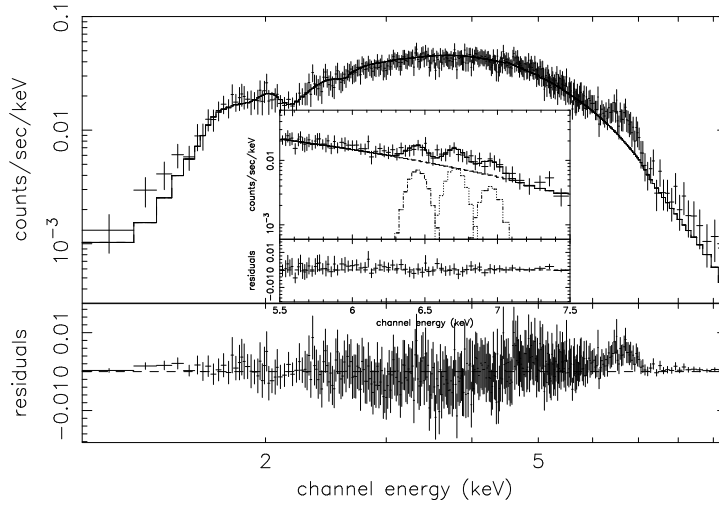


Fig. 5.— Significantly different line emission in the 0.8-1.0 phase bin between the two observations. (left) Observation 1: the 6.4 keV and 6.68 keV lines are clearly visible, as is the 4.8 keV line (See §3.4). (right) Observation 2: no lines are visible. The continuum temperature has been fixed at 30 keV as described in the text.

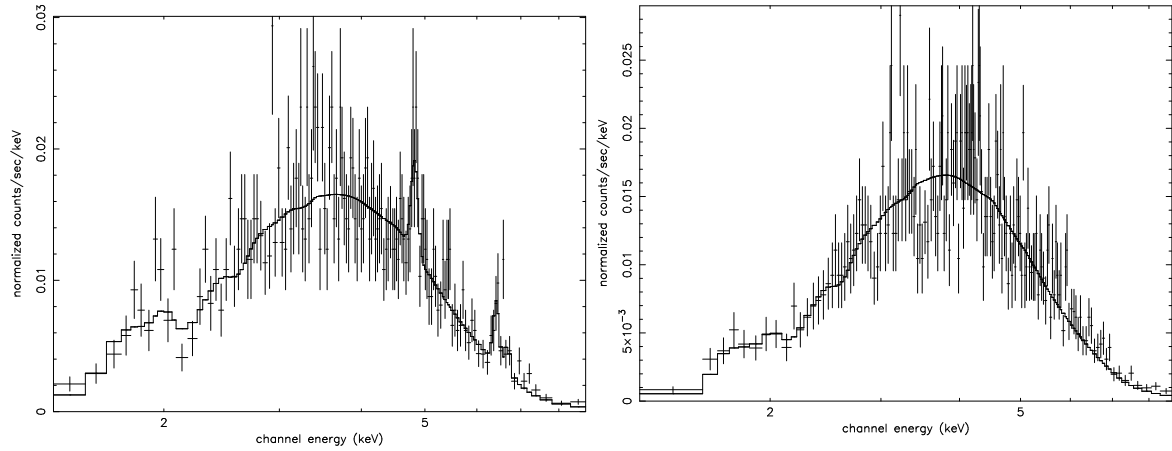


Fig. 6.— Changes in absorption during each orbit period. Open squares represent the first observation and filled blocks represent the second observation. The data have been repeated twice for clarity. This plot confirms an earlier study using *Ginga* (Kamata & Koyama 1993).

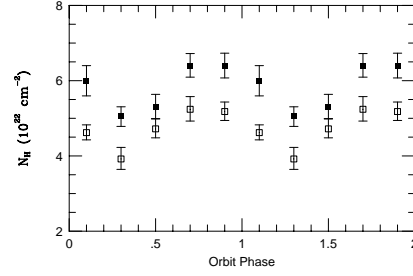


Fig. 7.— Changes in absorption during each spin period. Open squares represent the first observation and filled blocks represent the second observation. The data have been repeated twice for clarity.

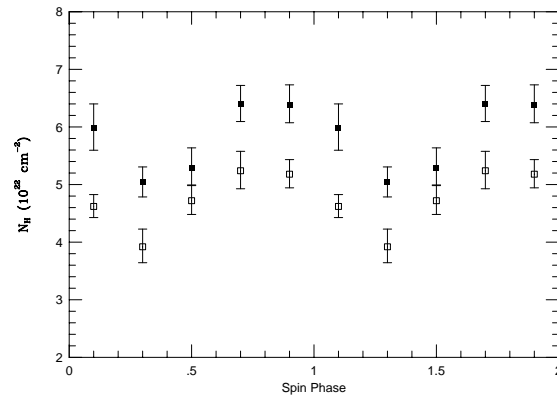


Fig. 8.— Changes in equivalent width during each spin period for the 6.40, 6.68, and 6.96 keV lines. Open symbols represent the first observation and filled symbols the second. Triangles represent upper limits. The data have been repeated twice for clarity.

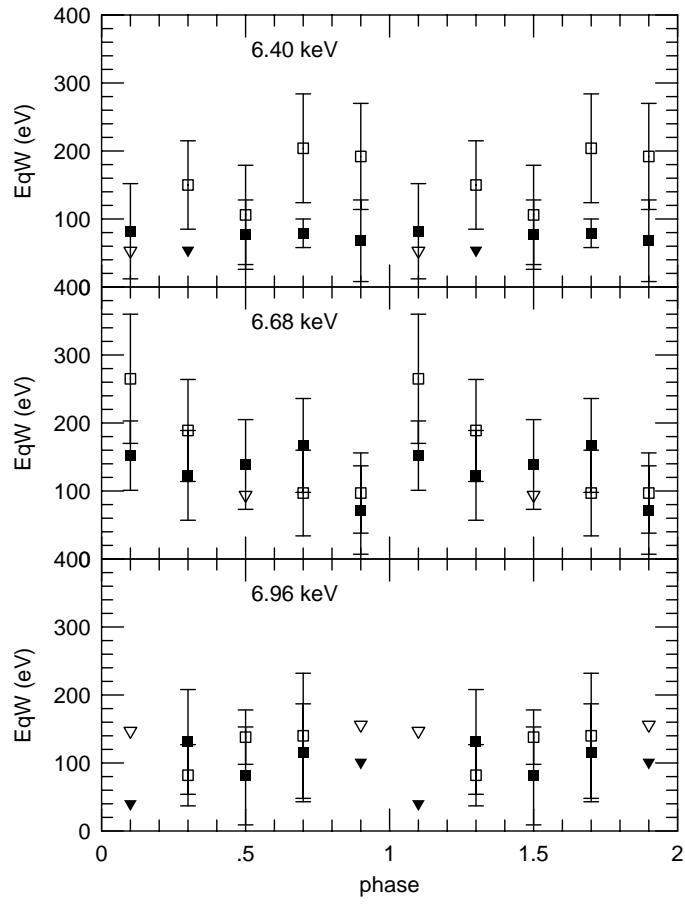


Table 2: Complete Data Sets: Combined/Weighted Data, First Observation, Second Observation¹

Data Set	Flux 2.0-10.0 keV (10^{-12} ergs/cm ² /s)	Column Density (10^{22} cm ⁻²)	Line Energy (keV)	Equivalent Width (eV)
Combined	$36.35^{+0.91}_{-0.88}$	$5.30^{+0.10}_{-0.10}$	$6.40^{+0.05}_{-0.03}$ $6.68^{+0.05}_{-0.08}$ $6.92^{+0.05}_{-0.05}$ $8.20^{+0.03}_{-0.18}$	108 ± 38 106 ± 46 117 ± 51 90 ± 51
First Observation	$18.27^{+0.38}_{-0.41}$	$4.60^{+0.11}_{-0.11}$	$4.88^{+0.10}_{-0.11}$ $6.41^{+0.06}_{-0.02}$ $6.66^{+0.04}_{-0.06}$ $6.96^{+0.05}_{-0.08}$	48^{+23}_{-40} 133^{+37}_{-46} 106^{+36}_{-44} 103^{+51}_{-64}
Second Observation	$18.01^{+0.32}_{-0.30}$	$5.65^{+0.12}_{-0.12}$	$6.44^{+0.08}_{-0.06}$ $6.69^{+0.07}_{-0.04}$ $6.91^{+0.05}_{-0.08}$ $8.12^{+0.08}_{-0.10}$	76^{+50}_{-36} 157^{+40}_{-50} 104^{+28}_{-54} 104^{+78}_{-71}

¹We adopted an absorbed thermal bremsstrahlung model for the continuum with a fixed temperature of 30 keV. All errors are 95% errors unless otherwise stated.

Table 3: 3-Bin Spin Phase Spectral Parameters¹

Phase	Unabsorbed Flux ²	Column Density ³	Equiv. Width (eV): line at __ keV			
			6.40	6.68	6.96	7.20
Observation 1						
0.3-0.6	4.62 ± 0.18	4.74 ± 0.18	120 ± 56	98 ± 51	147 ± 75	< 98
0.6-0.9	5.19 ± 0.23	4.49 ± 0.19	199 ± 65	97 ± 51	125 ± 73	119 ± 93
0.9-0.3	4.39 ± 0.17	4.58 ± 0.19	118 ± 53	158 ± 66	53 ± 51	< 88
Observation 2						
0.3-0.6	5.15 ± 0.17	5.15 ± 0.20	47 ± 42	116 ± 47	121 ± 63	< 86
0.6-0.9	5.05 ± 0.21	6.46 ± 0.26	91 ± 43	172 ± 57	162 ± 59	< 73
0.9-0.3	4.83 ± 0.18	5.77 ± 0.23	110 ± 54	68 ± 54	120 ± 72	< 87

¹We adopted an absorbed thermal bremsstrahlung model for the continuum with a fixed temperature of 30 keV. Line widths have been fixed at zero for all phases to approximate unresolved lines. All errors are 95%.

²in units of 10^{-12} (ergs/cm²/s) in the energy range 2.0-10.0 keV.

³in units of $N_H \times 10^{22}$ cm⁻².

Table 4: 5-Bin Spin Phase Spectral Parameters¹

Phase	Unabsorbed	Column	Equiv. Width (eV): line at __ keV		
	Flux ²	Density ³	6.40	6.68	6.96
Observation 1					
0.0-0.2	2.98±0.09	4.62±0.23	<53	265±95	<147
0.2-0.4	3.07±0.14	3.92±0.19	150±65	189±75	82±45
0.4-0.6	3.26±0.14	4.72±0.25	106±73	<94	138±40
0.6-0.8	3.08±0.09	5.24±0.30	204±80	97±63	140±92
0.8-1.0	3.22±0.09	5.18±0.27	192±78	97±59	<156
Observation 2					
0.0-0.2	3.42±0.10	5.98±0.39	82±61	152±84	<40
0.2-0.4	3.23±0.11	5.05±0.24	<54	123±66	131±77
0.4-0.6	3.63±0.13	5.29±0.33	77±51	139±66	81±72
0.6-0.8	3.38±0.08	6.40±0.31	79±53	167±69	115±72
0.8-1.0	3.47±0.10	6.38±0.32	68±60	72±65	<101

¹We adopted an absorbed thermal bremsstrahlung model for the continuum with a fixed temperature of 30 keV. Line widths were fixed at zero for all phases. Errors on the equivalent widths are 1σ for comparison with values from the literature; other errors are 95%.

²in units of 10^{-12} (ergs/cm²/s) in the energy range 2.0-10.0 keV.

³in units of $N_H \times 10^{22} \text{ cm}^{-2}$.

Table 5: Unexpected Emission Lines in Observation 1¹

Line	Phase	EquivW	Upper Limits at			Line
Center	Observed	(eV)	$\Delta\chi^2$	Signif.	Other phases ²	Identity
3.25±0.04	0.2-0.4	44	5.5	94%	/36/.../27/24/77/	Ar K α 3.20 keV?
4.81±0.03	0.8-1.0	99	15.3	>99%	/41/81/37/30/.../	Ca XIX 4.832 keV?
5.39±0.04	0.0-0.2	85	7.8	97%	/.../85/86/40/117/	no id?

¹ Lines were fit using a gaussian of zero width to approximate an unresolved emission line.

² Upper limits at other phases: the 95% limits are defined at phases /0.0-0.2/0.2-0.4/0.4-0.6/0.6-0.8/0.8-1.0/ and in that order.